Available online at www.sciencedirect.com
ScienceDirect
Journal of Sound and Vibration 318 (2008) 830–849
JOURNAL OF SOUND AND VIBRATION
www.elsevier.com/locate/jsvi

Numerical simulation study of ground vibrations using forces from wheels of a running high-speed train

Masafumi Katou[a,*], Toshifumi Matsuoka[a], Osamu Yoshioka[b], Yoshinori Sanada[c], Takayuki Miyoshi[a]

[a]*Department of Civil & Earth Resources Engineering, Kyoto University, C1-1-109, Laboratory of Geological Engineering, Kyotodaigaku-Katsura, Nishikyo-ku, Kyoto 615-8540, Japan*
[b]*Technology Research and Development Department, Central Japan Railway Company, 1545-33 Ohyama, Komaki, Aichi 485-0801, Japan*
[c]*Center for Deep Earth Exploration, Japan Agency for Marine-Earth Science and Technology, 3173-25 Showa-cho, Kanazawa-ku, Yokohama, Kanagawa 236-0001, Japan*

Received 4 February 2008; accepted 27 April 2008
Handling Editor: L.G. Tham
Available online 13 June 2008

Abstract

A 3-D viscoelastic finite difference method (FDM) was adopted to study the mechanism of ground vibrations induced by a high-speed train. Time-series data of the forces acting on the railroad were observed from the wheels of a running Shinkansen train in Japan and were used to develop a realistic source function as an input to numerical simulations for a single wheel. This is because the measured forces include suitable frequency components. A 3-D numerical model of the embankment of the railroad was designed to mimic a test field site for which borehole logging data were available. Simple analytical discussions concluded that a rail length of 120 m and a grid spacing of 0.25 m were acceptable for stable FDM simulations without numerical dispersion, and a model with about 32 million grid points was adopted for this study. A staggered-grid FDM with fourth-order accuracy in space was used for the numerical simulations. Finally, the simulated ground vibration was compared with the observed vibrations at the test site. The simulated ground vibrations closely resembled the observed ones. At the test site, the quality factor (Q) was not observed experimentally; however, the best match with field data was realized by assuming $Q = 5$–50.

1. Introduction

The high-speed train generates vibration in ground near the rail track, which sometimes causes an environmental problem for people and structures in the wayside. It is thus significant to develop a theory that can quantitatively explain the train-induced ground vibration. The vibration is characterized by three factors: a moving load source, elastic or viscous properties of ground, and coupling between the source and the ground. Since the effects of the ground and the coupling can be basically explained by general elastic-wave theory [1], treatment of the moving load source remains a particular problem in this field.

*Corresponding author. Tel.: +81 75 383 3201; fax: +81 75 383 3203.
E-mail address: masafumi-katou@hotmail.co.jp (M. Katou).

0022-460X/$ - see front matter © 2008 Elsevier Ltd. All rights reserved.
doi:10.1016/j.jsv.2008.04.053

Previous research has indicated that the moving load source can be separated into two independent factors: a quasi-static moving source (SMS) and a dynamic moving source (DMS). Recently, the DMS has been recognized as a dominant factor in ground vibration, while the SMS is considered to be an effect of the weight of the running train as it pushes on the ground. Takemiya and Bian [2] concluded that the train weight could generate ground vibrations with components with frequencies less than 10 Hz and that these vibrations quickly decay with increasing distance from the rail track. The specific vibration caused by the sleepers under the rails is known as the sleeper passage vibration, and its frequency depends on the distance between the sleepers. Degrande and Lombaert [3] simulated low- and high-frequency vibrations in the near field generated by a quasi-static moving source and the effect of the sleeper passage source. Since the interval distance of sleepers is usually 50–60 cm, the sleeper passage frequency increases to 100 Hz when the train is running at a speed of 60 m s^{-1} or more. Thus, train weight is not the main factor in generating mid-frequency bands in the far field [3]. In theory, dynamic loads are significant compared to the bow wave generated from the train weight even in the case of trains traveling at speeds greater than the ground wave speed [4].

From the above studies, it is clear that the DMS problem needs to be studied more carefully since the observed vibrations are mainly between 5 and 40 Hz with an offset of 10–20 m away from the track, as demonstrated in the second section of this paper. Recently, Sheng et al. [5] and Lombaert et al. [6] estimated the DMS from train wheels using a combined model of rail track dynamics and track irregularity. Their simulated ground vibrations from this estimated source matched well with field observation records. However, the model parameters for rail, sleeper, ballast and soil might not be constant because the track had irregularities. Although the dynamics model proposed by them [5,6] is elaborate, acquisition of these model parameters is difficult. Therefore, in this paper we propose a direct approach to observe the dynamic force received by the ground from trains by using strain gauges on the wheels.

Many researchers have employed Green's functions for a layered half-space for the evaluation of elastic/viscoelastic wavefields in the frequency domain. Recently, many new methodologies for calculating 3-D space have been proposed for the evaluation of 3-D structures (e.g., embankments and viaducts) [7–10]. Hall [7] adopted a finite element method that can evaluate complex surface topography. O'Brien and Rizos [8] proposed a finite element method and boundary element method (FEM–BEM) that considers rail–sleeper interactions. Sheng et al. [9] proposed a wavenumber finite and boundary element method (FE–BEM) that can handle an embankment structure. Takemiya and Bian [10] applied the finite element method (FEM) to the viaduct–ground interaction. These methodologies might become important tools in the future because they can precisely handle complex structural problems. In this study, the time domain finite difference method (FDM) with staggered-grid arrangement was used for the simulation. As described in Section 4, this method offers many advantages.

As in the case of Lombaert et al. [6], the purpose of this paper was to reproduce the observed ground vibration as precisely as possible. Based on the above background information, in this study the transient forces from the train to the tracks were observed by using strain gauges mounted on the wheels. Next, 3-D numerical wavefield simulations were conducted by using these forces as the moving load source. The observed force on the train wheels can be considered to be the same as the force acting on the soil surface because of the law of action–reaction. Moreover, the observed data contained suitable frequency components. A 3-D numerical model was designed to mimic a real field site that included an embankment for which borehole logging data and surface measured seismograms were available. Numerical simulation resembled the observed ground vibration data qualitatively and quantitatively, and these data were reproduced at frequencies between 5 and 40 Hz and at 10–20 m away from the high-speed train track.

2. Observed ground vibrations and forces

In this section, the observed vibration data and the force acting on the wheel of a running train at a test field site are discussed. This force plays a major role in this study because it is used as the external force in the numerical simulations.

2.1. Line spectrum of ground vibrations

The test field site was along the Tokyo-Osaka Shinkansen line at Yasu, Shiga Prefecture, where the railway is straight and runs through rice fields with no external traffic or industrial noises. The site is an earth embankment, as shown schematically in Fig. 1. A vertical cross-section of the embankment is shown in the upper left of Fig. 1, which also shows the locations of the left and right wheels of a train running toward Tokyo. Fig. 2 shows an image taken from location B toward A in Fig. 1. Accelerometers were located on the road shown in the lower right of Fig. 2. The P wave (V_p) and S wave (V_s) velocities obtained at this site are given in Table 1 by using PS-logging data collected from a borehole near the field site (to the right of A in Fig. 2). Since V_p and V_s in the embankment and all material densities could not be observed directly, empirically estimated values were used.

We observed the ground vibration induced by a train passing at $V = 74.4\,\mathrm{m\,s^{-1}}$. Figs. 3(a) and (b) show the measured time series and the amplitude spectra, respectively, at locations A and B. These data represent the vertical acceleration component of the ground vibration (a_z). In Fig. 3(b), about 10 main peaks are recognized (8.9, 11.9, 17.9, 20.8, 23.8, 26.8, 29.7, 32.7, 35.6, and 38.6 Hz). These frequencies were determined by the train axle arrangement and the velocity of the running train, as explained below.

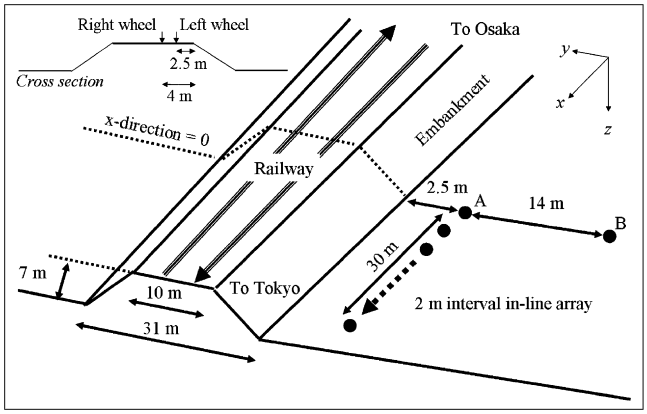

Fig. 1. Schematic illustration of the field site and simulation model. Upper left panel shows a cross section of the embankment. Locations of the right side and left side wheels are indicated.

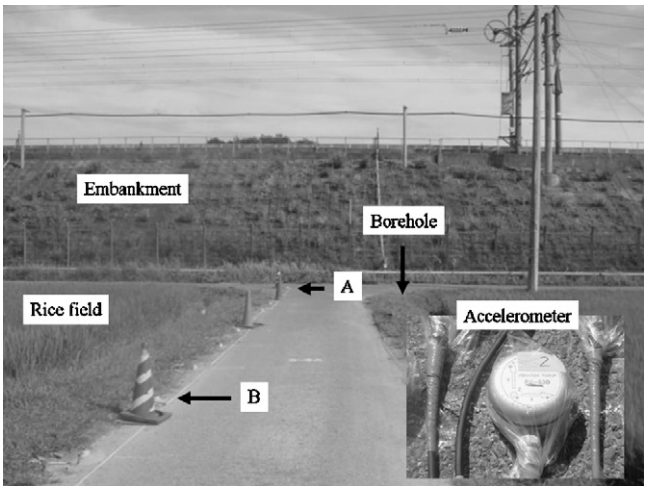

Fig. 2. Picture of the field site taken from location B in Fig. 1. Lower right inset is an image of the accelerometer.

Table 1
PS logging data from the Yasu site shown in Figs. 1 and 2

ID	Depth (m)	V_p (m s^{-1})	V_s (m s^{-1})	ρ (kg m^{-3})
0	Embankment	800	200	1400
1	0.00–1.75	1000	120	1500
2	1.75–3.50	1000	150	1500
3	3.50–5.00	1000	240	1500
4	5.00–7.75	1900	240	1500
5	7.75–11.5	1900	180	1500
6	11.5–13.5	1900	240	1500
7	13.5–14.5	1900	430	1500
8	14.5–	1900	580	1500

The borehole was to the right of location A in Fig. 2.

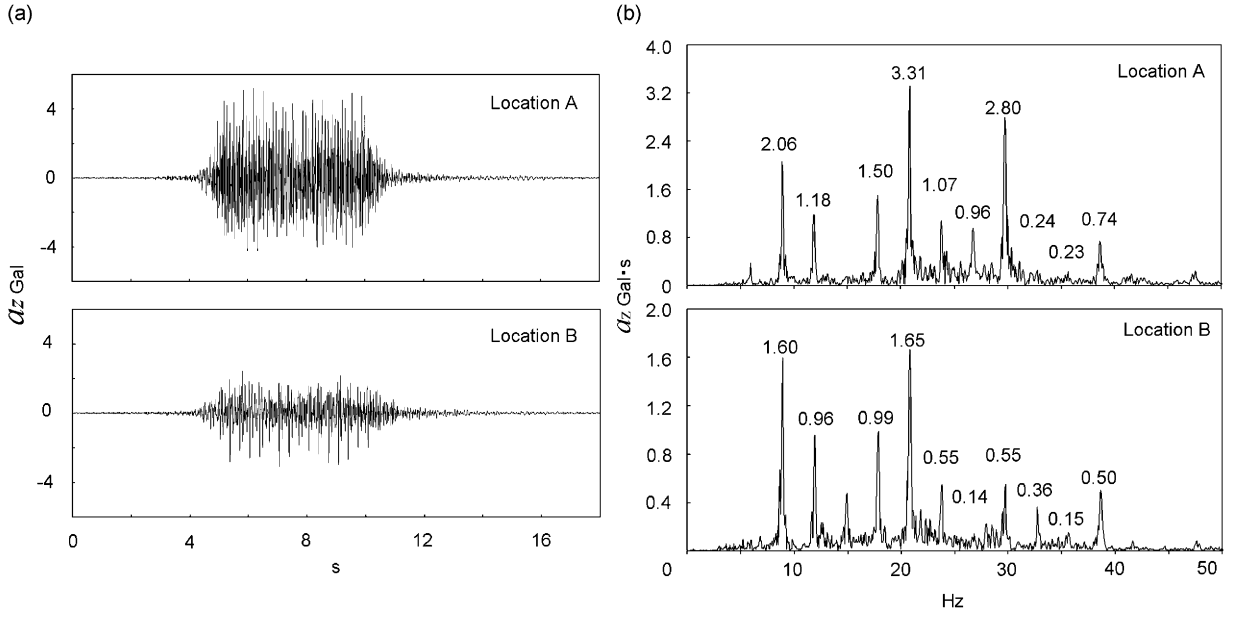

Fig. 3. (a) Time series from the field records of the vertical components of acceleration. Locations A and B were 15 and 30 m from the rail track, respectively. (b) Amplitude spectra for (a). Ten peak frequencies are indicated and are at 8.9, 11.9, 17.9, 20.8, 23.8, 26.8, 29.7, 32.7, 35.6, and 38.6 Hz.

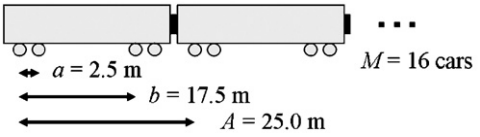

Fig. 4. The axle arrangement of the train.

The Shinkansen train consists of 16 cars and 64 axles, as shown in Fig. 4. Its bogie axle base is $a = 2.5$ m, bogie-center distance $b = 17.5$ m, car length $A = 25.0$ m, and number of cars $M = 16$. Each car has two bogies, each bogie has two axles, and each axle has a set of left and right wheels. If every axle generates the same wavefield, the total wavefield in the frequency domain $\tilde{g}(\omega)$ is the superposition of all wavefields

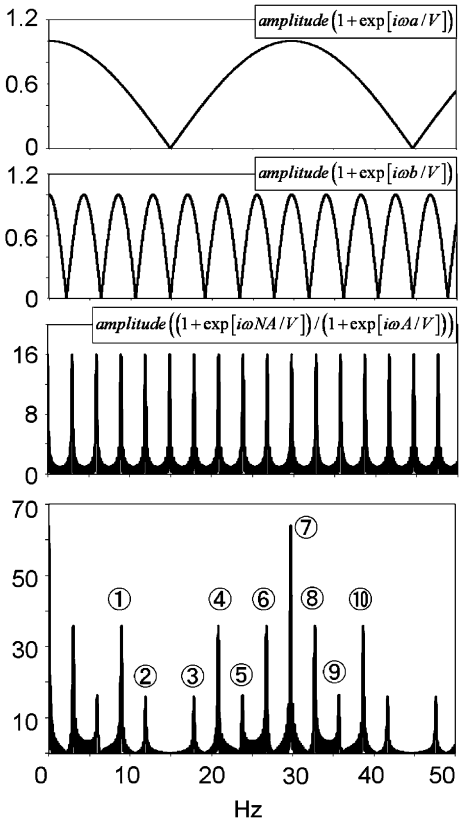

Fig. 5. The amplitude values of Eq. (1). By multiplying the top three panels, the bottom panel is obtained. The bottom panel shows the line-shaped envelope given by a 16-car train passing at 74.4 m s^{-1}. Ten main peak frequencies listed in Fig. 3 can be seen.

from individual wheels:

$$\tilde{g}(\omega) = \tilde{u}(\omega)\left\{1 + \exp\left[\mathrm{i}\omega\frac{a}{V}\right]\right\}\left\{1 + \exp\left[\mathrm{i}\omega\frac{b}{V}\right]\right\}\frac{1 + \exp[\mathrm{i}\omega(MA/V)]}{1 + \exp[\mathrm{i}\omega(A/V)]}, \tag{1}$$

where $\tilde{u}(\omega)$ is the response from a single axle [11].

Fig. 5 shows how the amplitude spectrum of $\tilde{g}(\omega)$ was obtained for the case of $V = 74.4\,\mathrm{m\,s^{-1}}$ and $\tilde{u}(\omega) = 1$. From the amplitude spectra of the three terms of Eq. (1), $(1 + \exp[\mathrm{i}\omega a/V])$, $(1 + \exp[\mathrm{i}\omega b/V])$, and $(1 + \exp[\mathrm{i}\omega MA/V])/(1 + \exp[\mathrm{i}\omega A/V])$, it can be seen that the third term strongly controls the features of the amplitude spectrum causing it to assume a line spectrum structure. The frequencies of these line spectra are the same as in the observed data of Fig. 3(b) within the frequency band between 9 and 40 Hz bounded by the instrument response for data acquisition. However, a 14.9-Hz peak was detected at point B. This may be because the response from each axle was not completely the same. When the distance from the track is increased, the contribution of the third term becomes stronger than the first two terms. The 3-D dynamics of the train body will be investigated in a future study to determine why the 14.9 Hz peak was observed at point B.

2.2. Doppler effect

As is well known, when studying vibrations induced by a moving source, the Doppler effect must be considered. This effect is described in the f–k domain as

$$f = Vk + f_0, \tag{2}$$

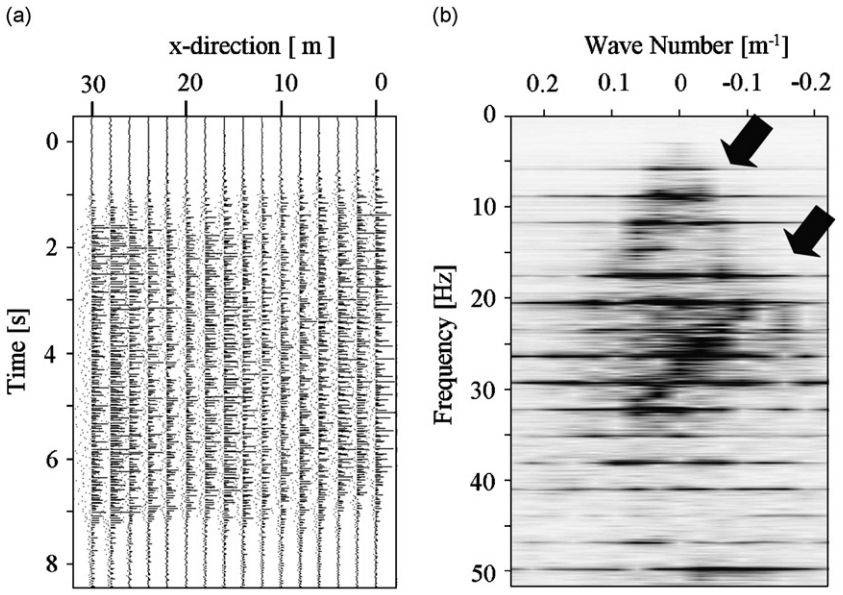

Fig. 6. Field data from the in-line array of 16 receivers arranged parallel to the railway shown in Fig. 1. (a) Vertical component acceleration waveforms for the test field. (b) The f–k spectrum. The sloping distributions indicated by arrows result from the Doppler effect.

where k (m^{-1}) is the wavenumber in the railway-parallel direction, V is the train speed ($m\,s^{-1}$), and f_0 is the frequency as measured on the running train. If the Doppler effect exists in the observed data, from Eq. (2) the f–k spectrum should exhibit a sloping distribution with angle V.

To investigate this effect, 16 receivers were arranged in a 2-m interval in-line array (Fig. 1). Fig. 6(a) shows the waveforms observed at the 16 receivers for a train passing at 73.2 $m\,s^{-1}$ toward Tokyo, and Fig. 6(b) shows the f–k spectrum of the waveforms. Sloping distributions with relatively strong amplitudes can be seen. As is discussed in more detail in Section 5, the Doppler effect is thus observed, so the wavefield is not generated from some specific points such as rail joints or defects. In fact, there is no rail joint within this test site.

2.3. Force acting on the wheels of a running train

The force acting on the wheels is measured for the purpose of the research regarding train dynamics. The procedure for this measurement was described in RTRI [12]. Fig. 7(a) shows 16 strain gauges attached to the wheel and Fig. 7(b) shows the connection diagram. This system can measure the vertical force on the wheel.

At the test site, the right and left wheel loads were observed and an interval 120 m in length was selected. Figs. 8(a) and (b) show the waveforms and amplitude spectra, respectively. Because there were 16 points where strain gauges were attached to the 0.43-m-radius train wheel, the sampling interval was 0.3377 m. Considering the Nyquist frequency, the available sampling interval of the measurements was 0.675 m and the data were interpolated using cubic spline functions. At a speed of 74.4 $m\,s^{-1}$, the train required 0.009 s to run a distance of 0.675 m; thus, 0.009 s was the sampling interval in the time domain. Therefore, the analyzable frequency band was less than 111 Hz, which was sufficient for this ground vibration problem.

From Fig. 8(a), the force acting on the wheel can be decomposed into a 47.7 kN average component and a ± 7 kN transient component. The decomposition of the total force into these two parts was important for the numerical studies that follow. As in many previous studies [2–6], these components can be labeled (1) the quasi-static moving source (SMS, 47.7 kN) and (2) the dynamic moving source (DMS, ± 7 kN). Note that 47.7 kN is 1/8 of the weight of a single car that has a total of eight wheels; therefore, the SMS corresponds to the train weight. The DMS term is about 10% of the total force acting on the railway track and is important in

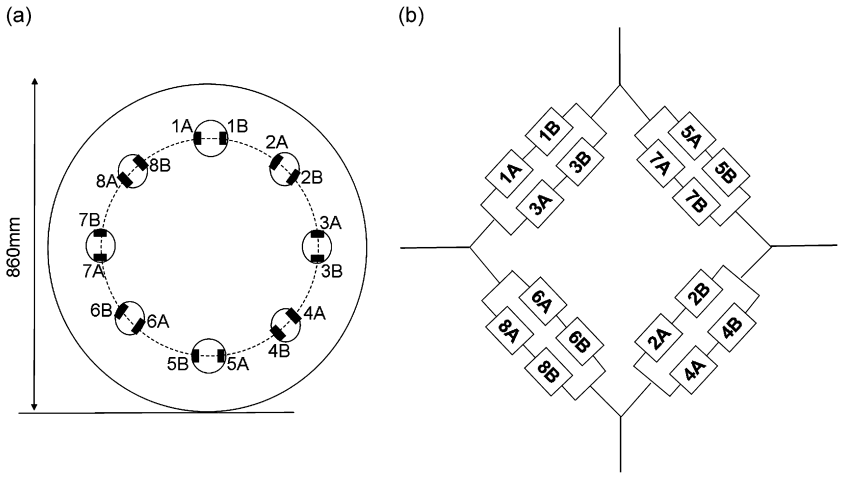

Fig. 7. (a) Diagram of a wheel with 16 strain gauges attached to measure the vertical force on the wheel. (b) Connection diagram.

predicting the ground vibrations. In the next sections, this force is directly used as the source for the numerical simulation.

As shown in Fig. 8(b), the DMS has 10 and 30 Hz components. The resonance of the axle part of Shinkansen train was about 50 Hz [13]. The origin of the DMS term is not completely clear, but the main factor must be track irregularity [5,6]. However, there could be many other factors such as the heterogeneity of the stiffness parameters under the rails, including the foundation ground, wheel irregularities, and aerodynamic effects.

3. Source waveforms of the ground vibrations

This section presents the procedure used to generate the input waveforms for numerical simulations by using the force measured by strain gauges attached to the wheels at the field test site (Fig. 8). According to the action–reaction law, the force received by the soil from the train is the same as the force on the wheel; however, the force-distribution effect due to the rail-sleepers has to be taken into consideration. Then we employed Krylov's [14] theory, which was validated by Takemiya and Bian [2] for an X-2000 Swedish high-speed train by comparing rail-displacement measurements and theoretical predictions. In addition, the manual for Japanese railway engineers [15] shows the results of track deflection measurements and estimates the theoretical parameters of Krylov [14].

After estimating the DMS by subtracting the SMS (= 47.4 kN) from the measured wheel load over the 120-m rail length, the distribution effect of a point force acting on the rail can be estimated from the following function:

$$\phi(x) = \frac{1}{\sqrt{2}Lc}\exp\left[-\left|\frac{x}{Lc}\right|\right]\sin\left[\left|\frac{x}{Lc}\right| + \frac{\pi}{4}\right], \tag{3}$$

where $Lc_c = \sqrt[4]{4EI/K}$. EI is the bending stiffness of the rail and K is the elasticity of the sleepers, ballast, and the railroad bed. In the case of a Shinkansen, Eq. (3) is normally employed [16–18], and $Lc = 4/(3\pi) \times 1.5$ (m) Fig. 9 schematically illustrates the procedure for making the input source waveforms. When a wheel is located at x_a at time t, the force delivered to the ground surface under the track at the point x_b is

$$F(x_a)\int_{x_b-(S/2)}^{x_b+(S/2)} \phi(x - x_a)\,\mathrm{d}x, \tag{4}$$

where $F(x)$ is the DMS term derived from the force in Fig. 8(a).

By advancing one time unit Δt in the numerical simulation, these integral values are reevaluated and the corresponding forces are obtained. Finally, a time series for all grid points x_b is obtained; an example of the

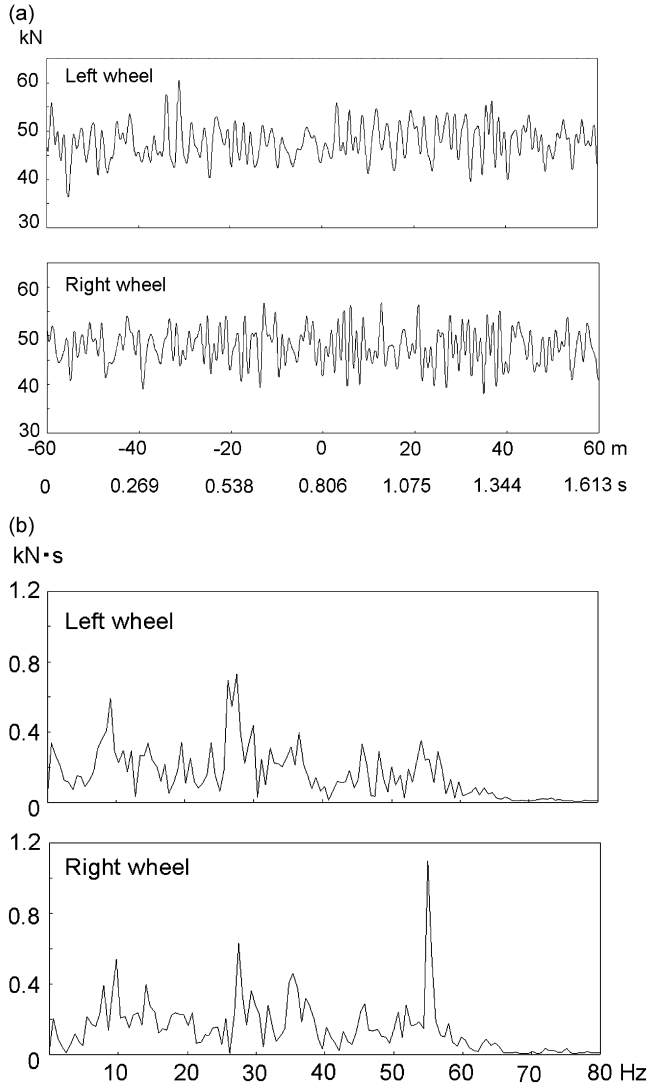

Fig. 8. Forces on left and right wheels of a train running at 74.4 m s^{-1}, which therefore covered 120 m in 1.613 s. (a) Waveforms. The horizontal axis distance corresponds to the x axis in Fig. 1. (b) Amplitude spectra made by the transient component of the time series.

input source waveforms is shown in the lower panel of Fig. 9. The time series for the left and right wheels become the input sources at the rail location for both wheels shown in the upper left of Fig. 1.

4. Finite difference method

4.1. Numerical model

The viscoelastic wave equation and the 3-D FDM [19] were used to compute the ground vibration propagation. A staggered grid with fourth-order accuracy in space was adopted for the grid scheme. In addition, the method of Cerjan et al. [20] was used for the absorbing boundaries on both sides and the bottom of the model. The authors originally investigated the computational performances between the FDM and the FEM and found that the FDM offered many advantages [21]. The programming schemes of the FDM are quite simple, and the FDM performs much faster and with lower memory usage than the FEM. The accuracy of the FDM is comparable to that of the FEM even when the calculation model includes a free surface. At the

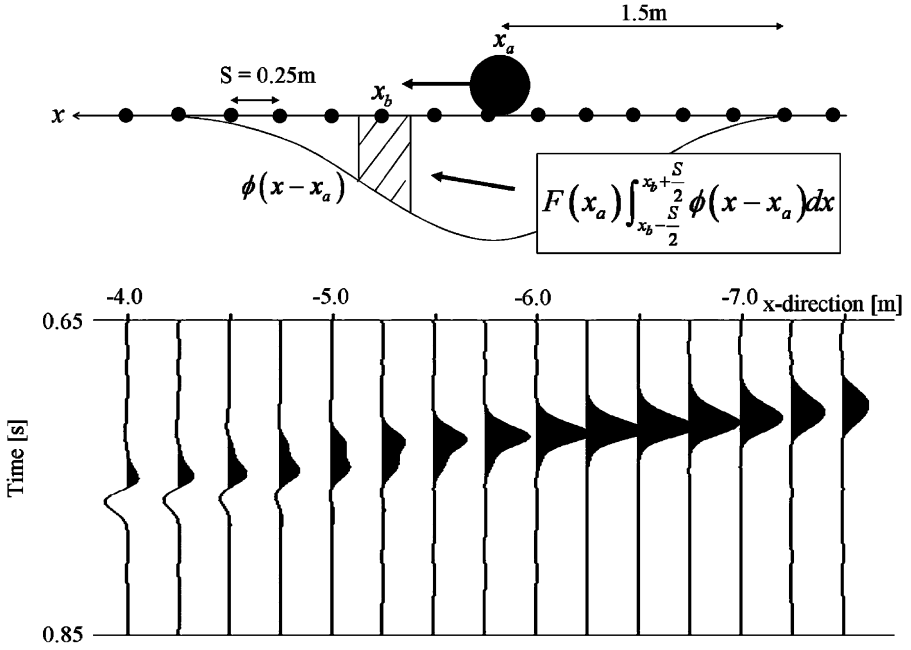

Fig. 9. Upper: Force distribution function of Eq. (3). Lower: Time series of the input waveforms.

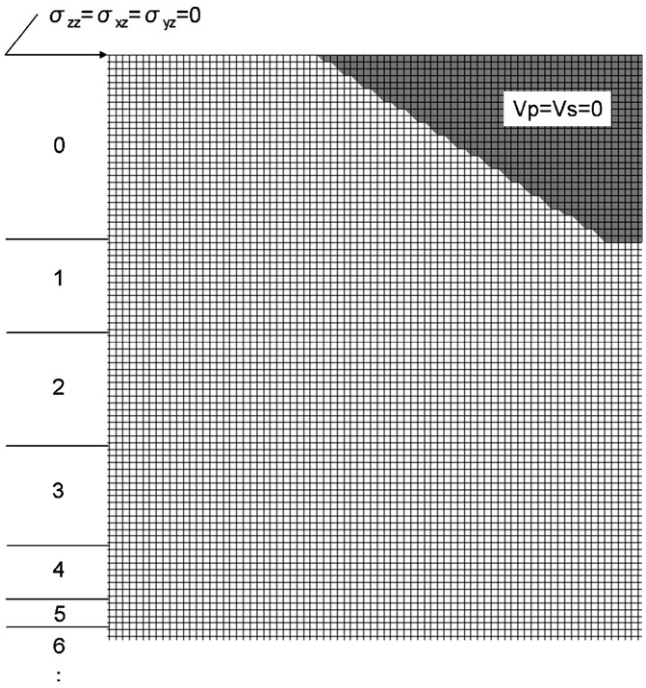

Fig. 10. Illustration of the FDM pixel arrangement.

top of the grid (free surface), two boundary conditions were employed: along the top of the embankment, the stress was set to zero [22]. At the surface, both V_p and V_s were set to zero; this is known as the vacuum formulation [23]. Hayashi [24] demonstrated that this combined free-surface boundary condition is the most

accurate FDM solver to express a model comprising surface topography. Fig. 10 illustrates the FDM calculation model. The ID numbers of the layers in Table 1 are indicated in the figure. The definition of the material boundaries was explained in the previous research [24,25].

Since it was difficult to obtain the quality factors Q_p and Q_s at the field site, the following six different Q value cases were evaluated: $Q_p = Q_s = 15.0, 25.0, 50.0$ at a central frequency of 15 Hz and $Q_p = Q_s = 5.0, 6.0, 7.5$ at 30 Hz. These values were selected based on the experienced intuition that at higher frequencies, the attenuation becomes stronger. To introduce viscoelastic wave equations, a physical model was required. The Zener model is an appropriate physical model to approximate a frequency-independent Q (Ref. [1], p. 172). Using the Zener model with one relaxation mechanism, the quality factor Q is defined as

$$Q(\omega) = \frac{Q_0 I_1}{I_0} \frac{1 + (\omega/\omega_0)^2}{\omega/\omega_0}, \tag{5}$$

where

$$I_0 = \frac{\omega_0}{2} [\ln\{1 + (\omega/\omega_0)^2\}]_{\omega_a}^{\omega_b}, \quad I_1 = \frac{\omega_0}{2} \left[\arctan(\omega/\omega_0) - \frac{\omega/\omega_0}{1 + (\omega/\omega_0)^2} \right]_{\omega_a}^{\omega_b}$$

in which $\omega_a = 1/2 \times \omega_0$ and $\omega_b = 3/2 \times \omega_0$ are the integral limits, and ω_0 is the viscosity central frequency [26]. In this case, the Q values (Q_0) are relatively frequency-independent over the range $0.5–1.5\omega_0$. Leurer [27]

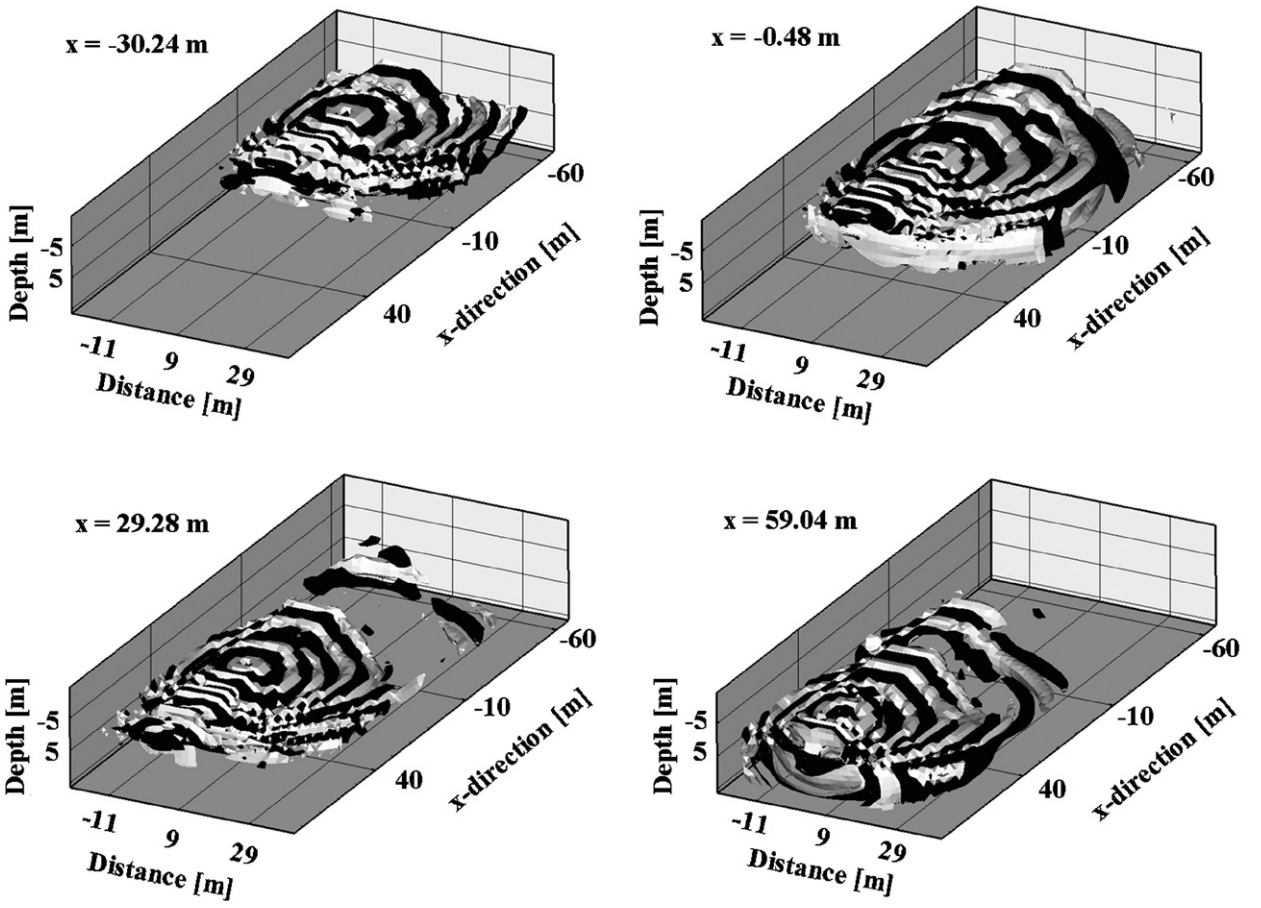

Fig. 11. Wavefield snapshots obtained by numerical simulation for various locations of a single axle. The plots are the isosurfaces of the vertical component of the particle velocity.

obtained Q_p/Q_s and suggested that it is less than or equal to 1 when V_p/V_s is greater than 3 and under low-pressure conditions. Following Leurer's discussion, a value of $Q_p/Q_s = 1$ was assumed in this paper.

4.2. Computation cost and railway length

In Appendix A it is shown that the computation requires a grid-cell size of 0.25 m and grid dimensions of 640 grids in the railroad direction, 320 across the railroad direction, and 160 in the vertical direction; therefore, the simulation model was composed of over 32 million grids. The time step was 5.0×10^{-4} s, and the

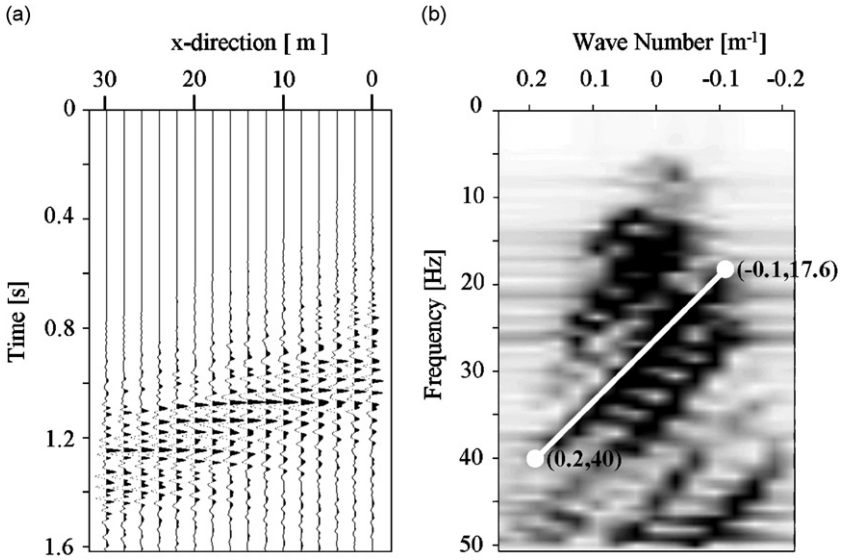

Fig. 12. (a) Vertical component acceleration waveforms obtained by numerical simulation. (b) The simulated *f–k* spectrum. The sloping distribution represents the Doppler effect described by Eq. (2).

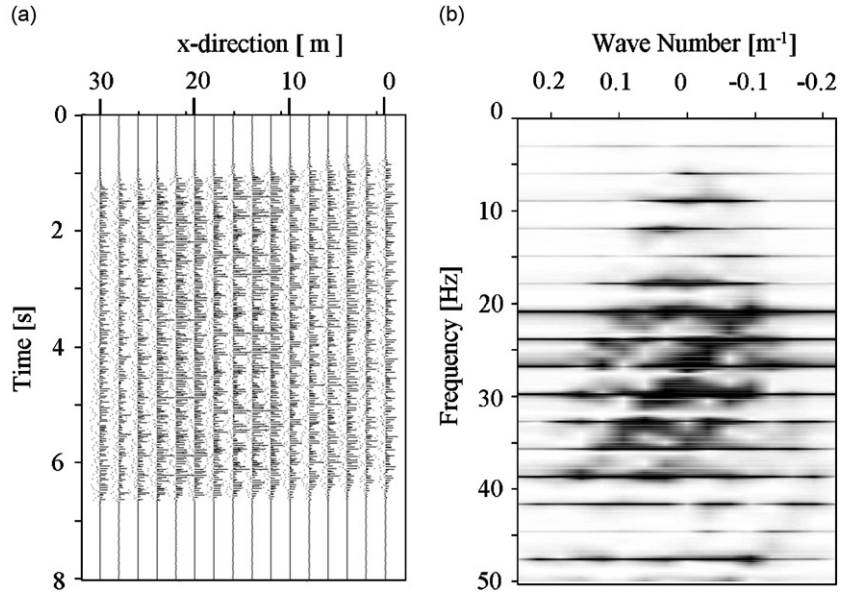

Fig. 13. (a) Superposed waveforms of Fig. 12(a), and (b) the total *f–k* spectrum. This aspect of the simulated spectrum is similar to the field data in Fig. 6.

calculation was done for 32 320 steps (time window of 1.616 s). These settings required 11 h of computation time using an HPC2500 super-computer in Kyoto University.

5. Results of numerical simulations and comparison with field data

In this section, the numerical simulation results such as wavefield snapshots, the f–k spectrum, and the amplitude spectrum of the wavefield are presented. In addition, these results are compared with the data observed at the test site. Two assumptions were made in these numerical simulations: first, ground vibration was induced by the DMS from the train, and second, the response from all the wheels of the Shinkansen train was the accumulation of the responses from a single axle.

5.1. Wavefield snapshots and f–k spectra

First, quantitative aspects such as wavefield snapshots and f–k spectra are discussed. The results obtained by numerical simulation with $Q_p = Q_s = 5.0$ at the central viscosity frequency of $\omega_0 = 30$ Hz were examined because this condition provided the best convergence of amplitude spectra among six values of Q, as is discussed in Section 5.2. Wavefield snapshots for various locations of a single axle (comprising right and left wheels) are shown in Fig. 11. Each plot shows the isosurface of the vertical component of the particle velocity, which forms roughly concentric circles. The waves ahead of the train are compressed and those behind are expanded. This phenomenon clearly shows the Doppler effect of the dynamic moving source.

Fig. 12(a) shows the simulated vertical component of the acceleration waveforms from one axle as would be detected by the in-line array of 16 receivers (Fig. 1). Fig. 12(b) shows the f–k spectrum of the simulated data. The spectral lobes show a linear slope (e.g., from points (−0.1, 17.6) to (0.2, 40)), which evidences the Doppler effect as described in the f–k domain by Eq. (2). Fig. 13(a) shows the total response from all 64 axles with the parameters in Table 1 and for a train speed of $V = 74.4\,\mathrm{m\,s^{-1}}$. Fig. 13(b) is the f–k spectrum, which is quite similar to the field record shown in Fig. 6. In conclusion, by comparing these two figures it is clear that the sloping distribution of the f–k spectrum in Fig. 6(b) is due to the Doppler effect observed at the test field site.

Table 2
Amplitudes from the field site data and the six simulations [Gal s]

Hz	Field	$Q = 50$ (15 Hz)	$Q = 25$ (15 Hz)	$Q = 15$ (15 Hz)	$Q = 7.5$ (30 Hz)	$Q = 6$ (30 Hz)	$Q = 5$ (30 Hz)
Location A							
8.9	2.06	1.24	0.98	0.80	0.52	0.43	0.31
11.9	1.18	0.69	0.59	0.54	0.63	0.57	0.52
17.9	1.50	2.05	1.64	1.36	1.12	0.97	0.82
20.8	3.31	15.25	12.57	9.96	5.52	4.19	3.19
23.8	1.07	3.19	2.41	1.82	0.82	0.63	0.47
26.8	0.96	17.60	14.60	11.62	5.42	4.08	3.03
29.7	2.80	5.79	4.31	2.70	1.46	1.33	1.12
32.7	0.24	5.37	4.51	3.44	1.55	1.06	0.76
35.6	0.23	5.39	4.34	2.93	0.11	0.17	0.13
38.6	0.74	11.54	7.65	4.41	1.33	1.08	0.94
Location B							
8.9	1.60	0.70	0.57	0.49	0.71	0.72	0.71
11.9	0.96	0.76	0.64	0.50	0.36	0.26	0.19
17.9	0.99	0.72	0.60	0.43	0.37	0.32	0.25
20.8	1.65	2.27	1.79	1.33	0.76	0.48	0.31
23.8	0.55	5.30	3.46	2.11	0.39	0.18	0.08
26.8	0.14	8.31	5.52	3.36	0.63	0.34	0.19
29.7	0.55	15.91	11.03	6.91	1.38	0.73	0.39
32.7	0.36	6.99	4.82	3.38	0.66	0.34	0.18
35.6	0.15	5.48	4.16	2.87	0.50	0.26	0.14
38.6	0.50	18.64	12.37	7.64	0.76	0.37	0.20

5.2. Amplitude spectra and time series

Six cases simulated by changing the quality factor Q were evaluated. The same 10 dominant peak frequencies appeared in the simulated data as in Fig. 3(b). The amplitude values at the 10 peak amplitudes are listed in Table 2. Four of the cases are visualized in Fig. 14. They show the vertical component of particle acceleration for the simulated wavefield at the observed locations A and B.

Fig. 15 shows the time series data at location A obtained for field data (a) and simulation data (b). These time series data were obtained by combining two cases: $Q_p = Q_s = 50$ at 15 Hz ($0 \leqslant f \leqslant 20$) and $Q_p = Q_s = 5$ at

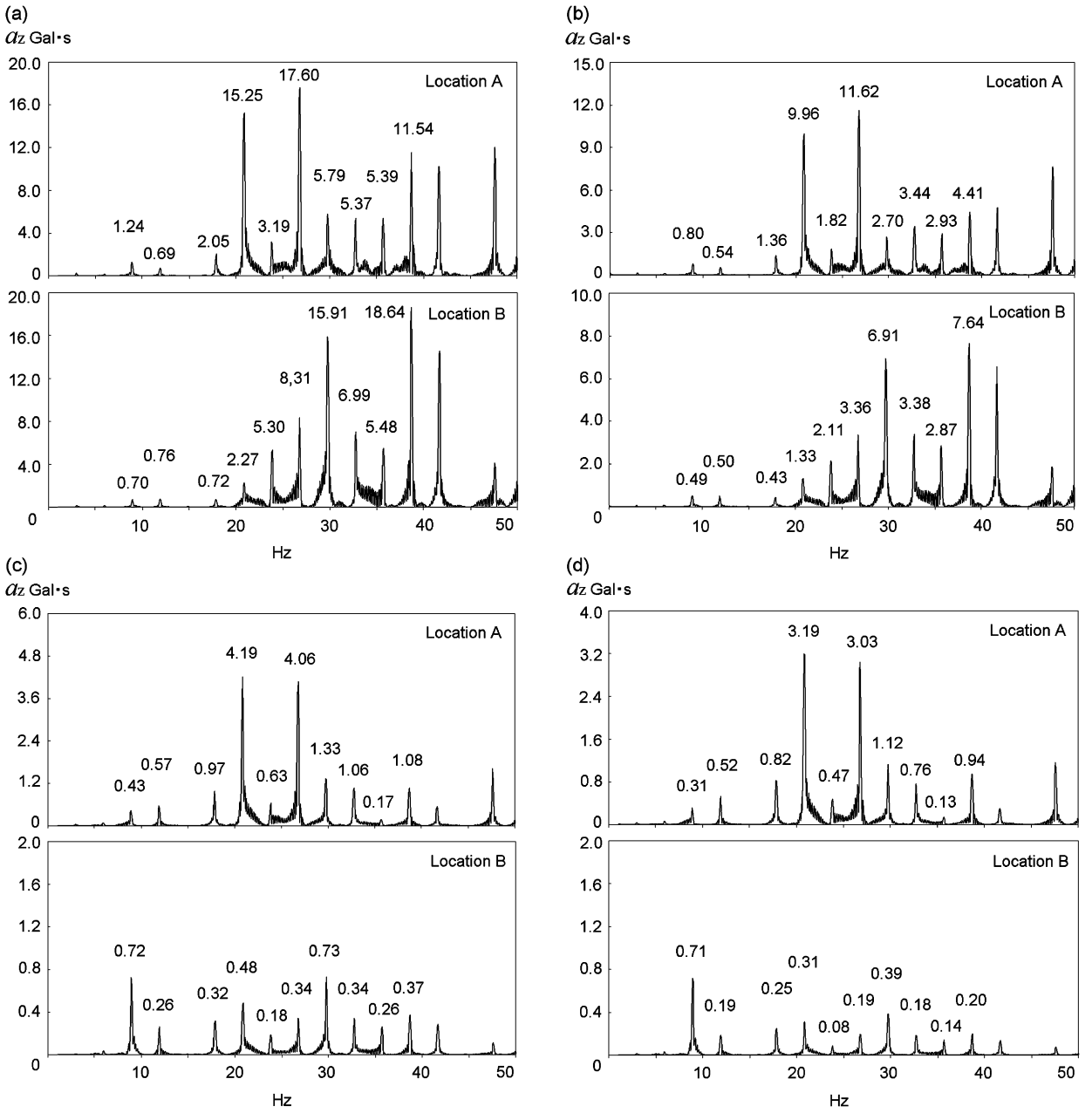

Fig. 14. Simulated ground vibrations for four separate Q settings. (a) $Q = 50$ and $\omega_0 = 2\pi \times 15$ Hz, (b) $Q = 15$ and $\omega_0 = 2\pi \times 30$ Hz, (c) $Q = 6$ and $\omega_0 = 2\pi \times 30$ Hz, and (d) $Q = 5$ and $\omega_0 = 2\pi \times 30$ Hz.

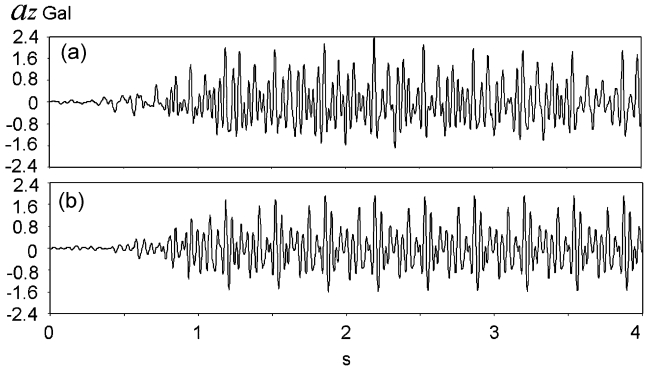

Fig. 15. Comparison of the simulated data with the field data in the time domain at location A. Simulation data were obtained by combining the two cases of $Q_p = Q_s = 50$ with $\omega_0 = 2\pi \times 15$ Hz ($0 \leqslant f < 20$) and $Q_p = Q_s = 5$ with $\omega_0 = 2\pi \times 30$ Hz ($20 \leqslant f \leqslant 40$). A 40-Hz low-pass filter was applied to both the simulated and field data.

30 Hz ($20 \leqslant f \leqslant 40$). The amplitude and phase characteristics of the simulated results are quite similar to the field data, including the absolute values of the vibrations.

6. Discussion

Overall, the simulation results were strongly controlled by the peak spectra identified in Fig. 5 and given by Eq. (1). These analyzable frequencies can be classified into two parts for descriptive purposes: the lower part, 0–15 Hz, including the two peaks of 8.9 and 11.9 Hz; and the higher part, 15–40 Hz, including the eight peaks of 17.9, 20.8, 23.8, 26.8, 29.7, 32.7, 35.6, and 38.6 Hz. In the higher frequency part, all three cases ($Q_p = Q_s = 7.5$, 6, and 5) match the field data. At the observed location A (the edge of the embankment), the case of $Q_p = Q_s = 5$ yields the best match with the field data. However, at location B (15 m from the embankment), the case of $Q_p = Q_s = 6$ gives the best match. This suggests that the attenuation effect of the embankment may be larger than that of the natural subsurface. In summary, when the frequency is higher, a numerical simulation with lower Q values gives the best match with field data. This low-Q tendency is typical in near-surface geophysics [28,29].

In the lower part, almost all of the six simulations show amplitudes weaker than the field data. From Appendix A, it can be inferred that the reason for this underestimation is the lack of railway length for the simulation. Another possible reason is that the geology differs away from the logging point, since lower frequencies generally propagate a longer distance than higher frequencies.

Contrary to the field data (Fig. 3(b)), the 14.9 Hz response at point B does not appear in the simulation. From Fig. 15, the field data have slightly more irregular waveforms than the simulation. This may suggest that each wheel is producing a slightly different wavefield. However, for practical purposes, the assumption that the response from every axle is the same is sufficient.

The observation of ground vibrations and the force on the wheel were not simultaneous, and the train used for the observation of ground vibrations was not the same as the train used for the measurement of force on the wheel. These differences could be among the causes of the mismatch between the simulation results and the observed data.

7. Conclusions

The observed ground vibrations induced by a Shinkansen train were studied. Exceptionally, the force on a wheel of a running train was considered, which was not easy to measure since a special wheel was required. The measurement, however, provided a useful data set for the simulation study. The measured force contained appropriate frequency components that could inherently reflect the irregularity in the railroad structures (e.g., rail, sleeper, ballast and soil). Using these measured forces, FDM simulations were conducted.

The simulation results reproduced all of the frequency components from 5 to 40 Hz, which were within the dominant frequency band causing environmental problems. In addition, the results revealed that the Doppler effect could be observed at the field test site. At a frequency of 15 Hz or higher, the observed vibration in the field test matched well with the numerical results in the case where $Q \leqslant 7.5$ and the soil of the test site is composed of strong damping materials. However, there were slight mismatches at 8.9 and 11.9 Hz caused by the lack of railway length for the simulation, or at 26.8 Hz by slight differences among the wavefields of the 64 axles.

In spite of the simplifying assumptions (i.e., the response from every axle was the same and only a dynamic moving source induced ground vibrations), the results adequately explained the observed ground vibration. On the other hand, there are cases where these assumptions cannot be applied. Moreover, attention should be paid to the amplification of vibration by building structures [30]. The FEM or BEM might become important tools since these methodologies can precisely handle complex structural problems. Because trains run on viaducts, particularly in urban areas, future studies should aim to develop a more efficient simulator that can handle a longer railway. The FDM simulation strategy of discretization and finiteness described in this paper will support future developments.

Acknowledgments

The authors appreciate the advice and support of Hitoshi Kanda and Hirotoshi Ishii of the Central Japan Railway Co. and Takashi Mitsuzuka of Chisitsu Keisoku Co. We would also like to thank Yuzuru Ashida and Hitoshi Mikada of Kyoto University, Adam O'Neill of DownUnder GeoSolutions, and Osamu Nishizawa of the National Institute of Advanced Industrial Science and Technology for their advice and encouragement.

Appendix A. Stability conditions for finite rail length

FDM simulations are conducted in a finite and discrete space. Thus, a continuous and infinite-length railroad must be approximated by a discrete and finite space. Using the Green's function for the acoustic wave equation, the analytical or semi-analytical response from a moving source can be evaluated. The analytical solutions supply the qualitative aspect of the response and the stability conditions for a moving source. Based on the discussions here, the FDM simulations were conducted under the conditions of a 120-m railroad length and 0.25-m grid spacing.

A.1. Average component of the force

First, the SMS (quasi-static moving source) part of the total force acting on the wheel is considered. The following assumptions are made: (i) the train runs at a constant speed on an isotropic homogeneous ground, and (ii) the running speed of the train is slower than the wave propagation velocity of the medium. In addition, it is assumed that the railway track is a straight line of infinite length.

The Green's function for the 2-D scalar wave equation in the frequency domain (Ref. [1], p. 190) is

$$G(r,\omega) = \frac{1}{r}\exp\left\{-\mathrm{i}\omega\frac{r}{c}\right\}, \tag{A.1}$$

where c is the propagation velocity of waves in the medium, i is the imaginary unit, and $r = \sqrt{x^2 + y^2}$. When a train runs in the positive direction on the x-axis with a constant speed, the source term of the 2-D scalar wave equation becomes a delta function given as the following moving source in the time domain:

$$f(x,0,t) = \delta(t - x/V), \tag{A.2}$$

where V is the velocity of the moving train. Then, the vibrational response from a moving source is written as the integration of the Green's function (Eq. (A.1)):

$$I = \int_{-\infty}^{+\infty} \frac{1}{r}\exp\left\{-\mathrm{i}\omega\left(\frac{r}{c} + \frac{x}{V}\right)\right\}\mathrm{d}x. \tag{A.3}$$

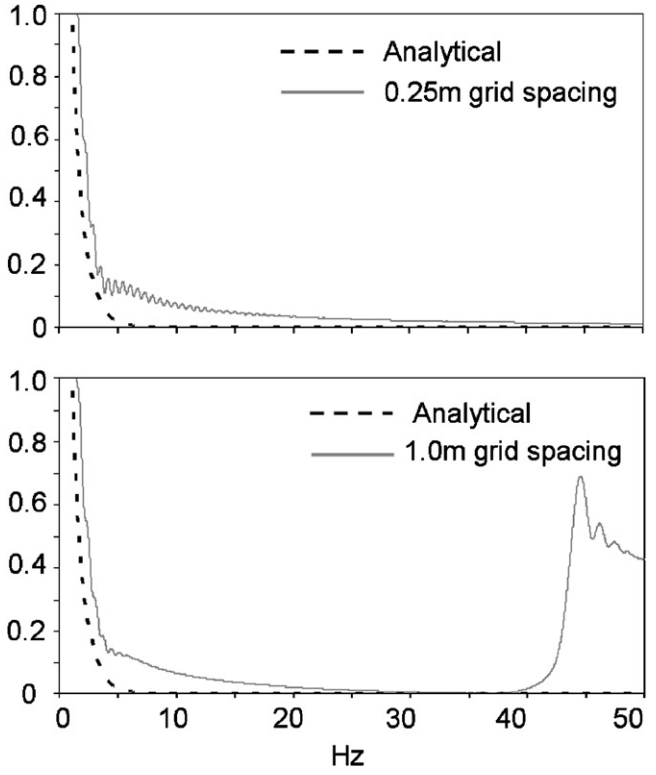

Fig. 16. Responses from the average component of force from a moving source in 2-D acoustic space. The analytical curve was obtained from Eq. (A.4) and approximate values from Eq. (A.5) under the conditions $c = 100\,\mathrm{m\,s^{-1}}$, $V = 75\,\mathrm{m\,s^{-1}}$, $y = 10\,\mathrm{m}$, and $S = 0.25\,\mathrm{m}$ or 1.0 m. The approximation of $S = 1.0\,\mathrm{m}$ manifests an error at 43 Hz or greater.

Since $V < c$, Eq. (A.3) becomes

$$I = 2K_0\left(\frac{\omega y}{c}\sqrt{\left(\frac{c}{V}\right)^2 - 1}\right). \tag{A.4}$$

Here, K_0 is the zeroth-order modified Bessel's function. The value of I in Eq. (A.4) is the analytical solution induced by a moving train with a constant load (SMS) running at a constant speed on an isotropic homogeneous medium.

The dashed line in Fig. 16 shows the value of I in the frequency domain when $c = 100\,\mathrm{m\,s^{-1}}$, $V = 75\,\mathrm{m\,s^{-1}}$, and $y = 10\,\mathrm{m}$. The amplitude response falls rapidly from 0 to 5 Hz and converges to zero. Because Eq. (A.4) does not have an imaginary part, there is no longer wave generation, but instead a deformation phenomenon of the medium is caused by the moving load. In other words, there are no vibrations since they are canceled by superposing all vibrational components generated by the running train. This suggests that under idealized conditions such as constant train speed and homogenous medium, the SMS does not induce any ground vibrations. Dunkin and Corbin [31] studied this zero-vibration phenomenon in 3-D elastic media.

A.2. Stability condition for grid spacing

For the numerical simulation, Eq. (A.3) is approximated in a finite length and discrete space as

$$I = \sum_{n=-N}^{N} \frac{S}{r_n}\exp\left\{-\mathrm{i}\omega\left(\frac{r_n}{c} + \frac{nS}{V}\right)\right\}, \tag{A.5}$$

where $r_n = \sqrt{(nS)^2 + y^2}$ and S is the grid spacing. In addition, N determines the finite railway length ($= 2N \times S$). Eq. (A.3) can be considered as describing the beating of the ground at movement speed V at

intervals of S. Therefore, discretization creates a vibrational component with frequency V/S. However, if this frequency is sufficiently high and out of the considered frequency band, this discretization strategy for examining the railroad (S value) is acceptable.

The absolute value of I in Eq. (A.5) is plotted for $N = 240$ and $S = 0.25$ m (length of railway is 120 m) as a gray solid line in the middle panel of Fig. 16, and the dotted line is the analytical solution of Eq. (A.4). For $N = 60$ and $S = 1.0$ m (same railway length), the absolute value of I in Eq. (A.5) is the solid line in the bottom panel of Fig. 16. When $S = 1.0$ m, vibrational components, due to the discretization of the moving load, appear above 43 Hz. Although V/S is 75 Hz in this case, the Doppler effect expands this simple harmonic oscillation to a frequency band 42.8–300 Hz according to the following equation:

$$\frac{c}{c+V}\frac{V}{S} < f < \frac{c}{c-V}\frac{V}{S}. \tag{A.6}$$

This implies that a continuous railway can be approximated by a discrete railway by using an appropriate discrete spacing. There are also discrepancies between the discretized results and the analytical solutions in the low frequency part for both the $S = 0.25$ m and $S = 1.0$ m cases. However, this discrepancy comes from the finite length (120 m) of the railroad and is not caused by the discretization.

As is well known, the FDM shows grid dispersion when the grid distance is large. The FDM with a staggered-grid scheme requires about 6–8 grids for the shortest wavelength [24]. When the velocity in the medium is specified, this leads to the maximum acceptable frequency of the source term, such as $\min\{c\}/7S$ for the 7-grid case. From the field site model in Table 1, when $\min\{c\}$ is 120 m s^{-1} and the grid distance is $S = 0.25$ m, this frequency is 68.6 Hz. By considering the Doppler effect, finally the maximum frequency condition of the vibration source to achieve stable results without grid dispersion is obtained:

$$f < \frac{1}{1+V/\min\{c\}}\frac{\min\{c\}}{7S}. \tag{A.7}$$

In the site model, 42.3 Hz is the maximum acceptable frequency.

Based on these discussions, the discretized SMS with $S = 0.25$ m does not induce any ground vibrations in a homogeneous medium in the frequency band considered.

A.3. Stability condition for the railroad length

Finally, the finiteness of the railway length is discussed. To make the condition more realistic, the following Green's function for a surface wave is employed:

$$G(r,\omega) = \frac{1}{\sqrt{r}}\exp\left\{-\frac{\omega r}{2Qc}\right\}\exp\left\{-\mathrm{i}\omega\frac{r}{c}\right\}, \tag{A.8}$$

where Q is the quality factor of the attenuation (the Green's function for the attenuating medium and the distance decay of the surface wave are described on pp. 174 and 215 in Ref. [1], respectively). Q is treated as frequency-independent. Although an analytical solution such as Eq. (A.4) cannot be obtained for Eq. (A.8), it is more realistic than Eq. (A.1) since the ground vibration considered in this paper is mainly a surface wave through a damping material.

Because the source function corresponding to the DMS is not a constant value such as Eq. (A.2), a single harmonic oscillation $\cos(x\omega_0/V)$ is evaluated as the source function of the DMS. Therefore, the following moving source function for the DMS case is employed:

$$f(x,0,t) = \delta(t - x/V)\cos(x\omega_0/V), \tag{A.9}$$

where ω_0 is the vibrational frequency of the moving train. Using Eqs. (A.8) and (A.9), the vibrational response from the DMS term is obtained as $(J+J')/2$, where J and J' are given by

$$J = \int_{-\infty}^{+\infty}\frac{1}{\sqrt{r}}\exp\left\{-\frac{\omega r}{2Qc}\right\}\exp\left\{-\mathrm{i}\omega\frac{r}{c}\right\}\exp\left\{-\mathrm{i}x\frac{\omega-\omega_0}{V}\right\}\mathrm{d}x \tag{A.10}$$

and

$$J' = \int_{-\infty}^{+\infty} \frac{1}{\sqrt{r}} \exp\left\{-\frac{\omega r}{2Qc}\right\} \exp\left\{-\mathrm{i}\omega \frac{r}{c}\right\} \exp\left\{-\mathrm{i}x \frac{\omega + \omega_0}{V}\right\} \mathrm{d}x. \tag{A.11}$$

Note that J' becomes a very small value in comparison to J when $\omega > 0$ under the condition $c > V$. Therefore, J' is negligible in the following discussions.

As with Eq. (A.5), Eq. (A.10) can be discretized into

$$J = \sum_{n=-N}^{N} \frac{S}{\sqrt{r_n}} \exp\left\{-\frac{\omega r_n}{2Qc}\right\} \exp\left\{-\mathrm{i}\omega \frac{r_n}{c}\right\} \exp\left\{-\mathrm{i}nS \frac{\omega - \omega_0}{V}\right\}. \tag{A.12}$$

Figs. 17(a) and (b) show the absolute values of J for the cases of $N = 2400$ (railway length 1200 m) and $N = 240$ (railway length 120 m), respectively. Here, $c = 100\,\mathrm{m\,s^{-1}}$, $Q = 10$, $V = 75\,\mathrm{m\,s^{-1}}$, $y = 15\,\mathrm{m}$, and $\omega_0 = 2\pi \times 20\,\mathrm{Hz}$. $Q = 10$ is an empirically appropriate value for modeling of the ground surface. The quality factor Q makes the amplitude decrease steadily with respect to the frequencies.

Fig. 17(c) shows the residual value between the 1200 and 120 m cases. Fewer than about 20% of the errors appeared lower than the cut-off frequency of the Doppler effect, which represents underestimation. Although these errors may not be small, the behavior of the response function in the high-frequency band

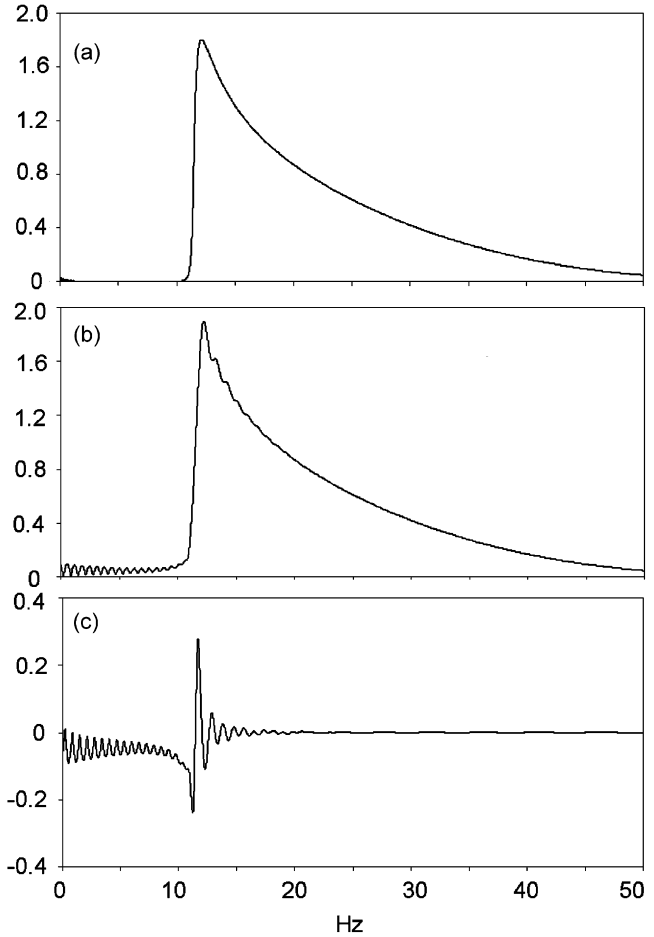

Fig. 17. Responses from the transient component of force from a moving source. The calculated medium had a viscosity with the quality factor $Q = 10$. An approximate value can be obtained with Eq. (A.12) under the conditions $c = 100\,\mathrm{m\,s^{-1}}$, $V = 75\,\mathrm{m\,s^{-1}}$, and $y = 15\,\mathrm{m}$. At 15 Hz or more, the 120 m railway approximation is the same as for 1200 m.

(15 Hz or more) is accurately evaluated. Although only the $\omega_0 = 2\pi \times 20\,\text{Hz}$ case is evaluated, Eq. (A.12) demonstrates that this acceptable frequency band is the same for any value of ω_0. From these considerations, a grid spacing of $S = 0.25\,\text{m}$ and a railroad length of 120 m were used for the FDM simulation study.

References

[1] K. Aki, P.G. Richards, *Quantitative Seismology*, second ed., University Science Books, Sausalito, CA, 2002.

[2] H. Takemiya, X. Bian, Substructure simulation of inhomogeneous track and layered ground dynamic interaction under train passage, *Journal of Engineering Mechanics ASCE* 7 (699) (2005).

[3] G. Degrande, G. Lombaert, An efficient formulation of Krylov's prediction model for train induced vibrations based on the dynamic reciprocity theorem, *Journal of the Acoustic Society of America* 110 (3) (2001) 1379–1390.

[4] X. Sheng, C.J.C. Jones, M. Petyt, Ground vibration generated by a load moving along a railway track, *Journal of Sound and Vibration* 228 (1999) 129–156.

[5] X. Sheng, C.J.C. Jones, D.J. Thompson, A theoretical model for ground vibration from trains generated by vertical track irregularities, *Journal of Sound and Vibration* 272 (2004) 937–965.

[6] G. Lombaert, G. Degrande, J. Kogut, S. Francois, The experimental validation of a numerical model for the prediction of railway induced vibrations, *Journal of Sound and Vibration* 272 (2006) 512–535.

[7] L. Hall, Simulations and analyses of train-induced ground vibrations in finite element models, *Soil Dynamics and Earthquake Engineering* 23 (2003) 403–413.

[8] J. O'Brien, D.C. Rizos, A 3D BEM-FEM methodology for simulation of high speed train induced vibrations, *Soil Dynamics and Earthquake Engineering* 25 (2005) 289–301.

[9] X. Sheng, C.J.C. Jones, D.J. Thompson, Prediction of ground vibration from trains using the wavenumber finite and boundary element methods, *Journal of Sound and Vibration* 293 (2006) 575–586.

[10] H. Takemiya, X.C. Bian, Shinkansen high-speed train induced ground vibrations in view of viaduct-ground interaction, *Soil Dynamics and Earthquake Engineering* 27 (2007) 506–520.

[11] O. Yoshioka, Some considerations on generating mechanism of vibration due to running trains, *BUTSURI-TANSA* 29 (1976) 23–33 (in Japanese).

[12] RTRI; Railway Technical Research Institute, *The Manuals and Interpretations to Speed up Conventional Railways*, Ken-yusha, Inc., 1993 (in Japanese).

[13] H. Kanda, O. Yoshioka, H. Ishii, M. Katou, Y. Sanada, T. Matsuoka, T. Miyoshi, Some remarks on source modeling in 3D simulation for wave field generated by moving loads, *BUTSURI-TANSA* 58 (4) (2005) 363–375 (in Japanese).

[14] V.V. Krylov, Vibrational impact of high-speed trains. I. Effect of track, *Journal of the Acoustic Society of America* 100 (5) (1996) 3121–3134.

[15] RTRI; Railway Technical Research Institute, *The Standard Design and Interpretations of Railway Structures for Soil Structures*, MARUZEN Publishing, 1992 (in Japanese).

[16] H. Takemiya, K. Goda, D. Komori, Computer simulation prediction of ground vibration induced by high-speed train running, *Journal of Geotechnical Engineering* 619 (I-47) (1999) 193–201 (in Japanese).

[17] H. Takemiya, S. Satonaka, W.P. Xiei, Train track-ground dynamics due to high speed moving source and ground vibration transmission, *Journal of Geotechnical Engineering* 682 (I-56) (2001) 299–309 (in Japanese).

[18] T. Hara, O. Yoshioka, H. Kanda, H. Funabashi, H. Negishi, Y. Fujino, K. Yoshida, Development of a new method to reduce Shinkansen-induced wayside vibrations applicable to rigid frame bridges: Bridge-end reinforcing method, *Journal of Geotechnical Engineering* 776 (I-68) (2004) 325–338 (in Japanese).

[19] J.O.A. Robertsson, J.O. Blanch, W.W. Symes, Viscoelastic finite-difference modeling, *Geophysics* 59 (1994) 1444–1456.

[20] C. Cerjan, D. Kosloff, R. Kosloff, M. Reshef, A nonreflecting boundary condition for discrete acoustic-wave and elastic-wave equations, *Geophysics* 50 (1985) 705–708.

[21] M. Katou, T. Matsuoka, H. Mikada, Y. Sanada, Y. Ashida, Simulation of the elastic wave propagation by 3D FEM with moving least square interpolants and parallel computing, *Abstract of ICCM2007, International Conference on Computational Methods*, Hiroshima, Japan, 2007, p. 122 (Full paper CD-ROM, G7-4).

[22] A.R. Levander, Fourth-order finite-difference P-SV seismograms, *Geophysics* 53 (1988) 1425–1436.

[23] R.W. Graves, Simulating seismic wave propagation in 3D elastic media using staggered-grid finite differences, *Bulletin of the Seismic Society of America* 86 (1996) 1091–1106.

[24] K. Hayashi, Variable Grid Finite-Difference Modeling Including Surface Topography, M.S. Thesis, Department of Earth, Atmospheric, and Planetary Sciences, Massachusetts Institute of Technology, 1999.

[25] J.O.A. Robertsson, A numerical free-surface condition for elastic/viscoelastic finite-difference modeling in the presence of topography, *Geophysics* 61 (1996) 1921–1934.

[26] J.O. Blanch, J.O.A. Robertsson, W.W. Symes, Modeling of a constant Q: methodology and algorithm for an efficient and optimally inexpensive viscoelastic technique, *Geophysics* 60 (1995) 176–184.

[27] K.C. Leurer, Compressional- and shear-wave velocities and attenuation in deep-sea sediment during laboratory compaction, *Journal of the Acoustic Society of America* 116 (4) (2004) 2023–2030.

[28] J. Xia, R.D. Miller, C.B. Park, G. Tian, Determining Q of near-surface materials from Rayleigh waves, *Journal of Applied Geophysics* 51 (2002) 121–129.
[29] S. Foti, Using transfer function for estimating dissipative properties of soils from surface-wave data, *Near Surface Geophysics* (2004) 231–240.
[30] H. Xia, N. Zhang, Y.M. Cao, Experimental study of train-induced vibrations of environmental and buildings, *Journal of Sound and Vibration* 280 (2005) 1017–1029.
[31] J.W. Dunkin, D.G. Corbin, Deformation of a layered, elastic, half-space by uniformly moving line loads, *Bulletin of the Seismic Society of America* 60 (1970) 167–191.